metals

MDPI

Article

Rear Weld Pool Thermal Monitoring in GTAW Process Using a Developed Two-Colour Pyrometer

Vinicius Lemes Jorge *, Issam Bendaoud, Fabien Soulié and Cyril Bordreuil

Laboratory of Mechanical and Civil Engineering (LMGC), University of Montpellier, 34090 Montpellier, France; issam.bendaoud@umontpellier.fr (I.B.); fabien.soulie@umontpellier.fr (F.S.); cyril.bordreuil@umontpellier.fr (C.B.)
* Correspondence: vinicius.lemes-jorge@umontpellier.fr

Abstract: New systems and methods to access the temperature of the melt pool in welding processes have been developed to study phenomena, monitor behaviours, and even be used in closed-loop control strategies. Concerning arc welding processes, the arc radiation might impose a challenge to measure the temperature. However, heat input is the key point for welding quality. This work aims to evaluate the feasibility and detect potentialities of accessing the thermal field from the rear weld pool in the GTAW process by using in-house developed equipment. The original system was conceptualized based on a previous bichromatic method. Experiments were carried out with and without the wire feed addition, and welding parameters were varied to explore its impacts on the temperature measurement. A strategy to select the regions of interest (ROIs) within the weld pool was created, and the mean temperature was calculated and correlated to the weld bead features. This strategy was able to overcome the challenges imposed by the electrode/nozzle reflection and the arc radiation during the welding. The rear weld pool thermal field was shown to be an important source of data to provide hints of the weld bead features. The mean temperature can indicate geometrical changes in the weld bead. Furthermore, the technique has the potential to be used as a promising real-time process monitoring tool.

Keywords: weld pool; thermal field; two-colour pyrometry; GTAW; rear weld pool monitoring

Citation: Jorge, V.L.; Bendaoud, I.; Soulié, F.; Bordreuil, C. Rear Weld Pool Thermal Monitoring in GTAW Process Using a Developed Two-Colour Pyrometer. *Metals* **2024**, *14*, 937. https://doi.org/10.3390/met14080937

Academic Editor: Zhengwei Li

Received: 29 July 2024
Revised: 13 August 2024
Accepted: 15 August 2024
Published: 16 August 2024

1. Introduction

Welding is a complex process that involves various physical and chemical transformations. It includes melting and solidifying metal, fluid motion, and vaporization, all triggered by the heat input. The quality of a seam depends on its geometrical and metallurgical properties, which are determined by the fluid movement and heat transfer experienced by the molten pool [1]. Therefore, the temperature distribution within the weld pool can be an important source of data to assess the quality of welded joints. Thermal monitoring techniques have been the object of interest and studied by several researchers. Non-contact methods have been employed to measure and monitor the temperature in arc welding processes, such as the use of infrared cameras as the most common approach [2–4]. When the material radiative properties are well known, high accuracy can be reached. However, the difficulty in determining the emissivity of melted materials is well known [5], which is a function of material composition, temperature, and surface features. To overcome this challenge, new temperature measurement methods have been developed and studied.

Coniglio et al. [6] showcased the temperature measurement of the weld pool by determining the polarization properties of the radiation in one wavelength. The measurement system is not dependent on surface emissivity, but it works only for the assumption that the refractive index of the materials is independent of temperature. However, this system is sensitive and it can be modified as a result of changes in both the degree of emission and the spatial orientation of the surface. Schöpp et al. [5] and Muller et al. [7] combined a near-infrared high-speed camera with a spectrometer. Based on radiation theory and

the measured spectrum, the temperature and emissivity are computed with the help of a least-square fitting. This punctual measurement is then used to calibrate the high-speed camera and to reconstruct the surface temperature distribution. Despite seeming effective and able to estimate the temperature and the emissivity during the process, Schöpp et al. [5] mentioned that slag formed on the surface can influence the emissivity and hence leads to local overestimations of the surface temperature. However, the method looks difficult to apply as a monitoring strategy. Beyond rendering a complex setup (synchronization between the camera and spectrometer), it always raises the challenge of emissivity dependence on the measurement orientation.

Another technique that is applied for measuring the temperature field of radiation targets is the dual charge-coupled device (CCD). Briefly, in this method, one commercial colour camera is used, and a relationship between two of its three spectral responses from the red/green/blue output channels is established based on Planck's law. Nevertheless, according to Yu et al. [8], when CCD is used in welding the measurement, precision can be affected by the spectral bandwidth response and also the material's emissivity uncertainty. To improve the CCD method accuracy, the authors developed a model by using a backpropagation neural network to measure the temperature field of the weld pool with the red/green output channel values. The authors achieved higher accuracy with a maximum relative fitting error of 0.38%, and a mean absolute error of 1.3277 °C. Myers et al. [9] also discussed about the uncertainties and limitations of the CCD method, mainly due to the camera's thermal sensitivity range and the slope of the ratiometric response curves obtained from the red/green channels.

An alternative method that has been widely used and that is of interest for this current work is the two-colour pyrometer (TCP). The details of this method will be discussed in Section 2. Monier et al. [10] evaluated this method's performance over pure material melting measurements. Three combinations of a couple of filters were evaluated. The authors stated that the selection of the wavelengths directly affects the uncertainties of the measurement, and the choice of the filters is the technical key point. A minimum global uncertainty of 6.21% was reached by the authors. Innovatively, Richter et al. [11] measured the weld pool temperature using the GMAW process directly pointing out the measurement system through the arc. The authors were able to measure the arc spectrum and select the narrow-bandwidth optical filters at wavelengths of lower arc intensity (suppression of the plasma radiation). On the other hand, despite not using the same method, Yu et al. [8] were not able to obtain molten pool monitoring data from the images captured in the arcing time, but only in a short-circuiting time. Schwarzkopf et al. [12] also employed a two-colour-thermography system that enables acquiring spatial and temporal temperature information for low-melting temperature ranges (<1200 K). The study demonstrates that temperature can be accurately determined despite variations in signal intensity and emissivity for objects emitting constant thermal radiation.

Alongside the development of thermal measurement techniques, several strategies and methods have been developed to study phenomena and monitor the process, and are even being used in closed-loop control strategies. Ngo Huu et al. [13] used the TCP method to confirm the Marangoni force activity in the weld pool with keyhole plasma arc welding. Monier et al. [14] also used this method to measure the surface temperature of the droplet in pulsed GMAW and establish a correlation to the surface tension. Richter et al. [11] proposed a study to associate the weld pool temperature to the estimation of the weld pool volume using a sensor developed based on TCP. Using CCD method, Myers et al. [9] employed thermal weld pool images to validate complex physics models. Moreover, Myers et al. [15] used the melt pool thermal field produced by a laser-directed energy deposition (L-DED) process to determine the effective absorptivity and temperature dependent coefficient of surface tension in a multi-physics model. To make it possible, the authors associated the thermal measurements to cross-sectional weld bead features.

The increasing usage of artificial intelligence (AI) methods in welding and additive manufacturing processes is still worth mentioning. In an extended review, Yu et al. [16]

showed and discussed the strategies that have been developed to monitor weld penetration and also the gaps in its advancements. According to the authors, various kinds of raw information sources have been tried for being used to predict the penetration state for different processes and applications. Regarding temperature measurements and the employment of AI, Yu et al. [17] developed a novel approach for measuring the weld penetration of variable groove weldments using CCD and a neural network. According to the authors, the method reaches a strong generalization ability and can be applied to the online measurement of welding penetration for weldments with various groove angles and sizes. Buongiorno et al. [18] conducted an experimental study using a sequence of near-infrared images from a laser welding process as input for a customized convolutional neural network. The aim was to develop an industrial diagnostic framework for detecting weld defects. The results showed that the neural network architecture was highly effective in classifying malfunctioning weld joints with an average accuracy of 99%. The authors emphasized the potential for integrating thermographic-based quality control frameworks across the production line, where fast and accurate recognition and safety assurance are essential industrial requirements. In the same context, Knaack et al. [19] conducted a study that intended to locate critical welding defects such as lack of fusion, sagging, lack of penetration, and geometric deviations of the weld seam. The authors used infrared images and laser welding as a process and employed a comprehensive scheme based on classical machine learning methods. In addition, state-of-the-art deep learning algorithms and manual features extraction were also used. The study showed that the weld defect recognition method can be applied to real-time applications that require low latency.

Given this context, the challenges surrounding thermal measurement methods in terms of reliability when the systems are applied to welding processes is notorious. Although there are already studies addressing the thermal features of the weld pool as a potential source of data, an evaluation of the rear weld pool thermal monitoring in the GTAW process right next to the arc radiation has not been referenced in the literature yet, to the knowledge of this work's authors. Besides the heat input being the key point for welding quality, it directly impacts the weld pool temperature and might be sensed by its rear part. Hence, the global aim of this work was to evaluate the feasibility and detect potentialities of accessing the thermal field from the rear weld pool in the GTAW process. Moreover, a second goal, which had a technical characteristic, was to develop a two-colour pyrometer that could be miniaturized and more easily embedded.

2. Methodology and Experimental Procedure

The methodology employed to reach this work's objective was based on the development (conceptualization, manufacturing, and assembling) of compact thermal measurement equipment from a previous bichromatic method [10]. To evaluate its performance in addition to exploring the feasibility of using the thermal rear weld pool strategy, bead-on-plate weldings were carried out with and without the wire feed addition, and welding parameters were changed in order to explore its impacts on the measurement. A strategy to select the regions of interest (ROIs) was fixed, and the mean temperature within these areas was calculated. To elucidate the potentialities of the strategy, the weld bead features were correlated to their respective mean temperature evolution during the welding.

2.1. Measurement Method

The two-colour pyrometer method relies on the principles of Planck's radiation law and the Stefan–Boltzmann law to accurately measure the temperature of a target object. According to Planck's radiation law, all objects emit electromagnetic radiation in a manner that depends on their temperature and spectral emissivity. Spectral emissivity refers to the efficiency with which an object emits radiation at different wavelengths. This efficiency varies with temperature and material properties. In the two-colour pyrometry method, two detectors sensitive to different wavelengths of radiation are used. These wavelengths are carefully chosen to correspond to regions where the spectral emissivity of the target

material changes significantly with temperature. By measuring the intensity of radiation at these two wavelengths, the ratio of their intensities can be correlated with the temperature of the object (effectively compensating the errors due to changes in emissivity). However, Schöpp et al. [5] mentioned that the temperature determination of hot metals is difficult and requires the knowledge of the emissivity in the temperature and wavelength range considered in the optical analysis. Methods, materials, and processes strongly influence the results, especially above the liquidus temperature. Consequently, reliable values for temperature and emissivity have to be determined in combination. Especially related to stainless steel (which is also used in this current work), Devesse et al. [20] presented a method for measuring the surface temperature distribution of a melt pool of AISI 316L stainless steel (SS) using hyperspectral imaging and showed that the emissivity was almost constant inside the melt pool, showing no significant dependence on temperature. The authors also cited that the measured temperatures were in good correspondence with the values reported in the literature for similarly sized melt pools, obtained using standard pyrometric techniques with a gray body assumption (in a range of 1800 K to 2000 K). These results confirm that the gray body hypothesis can be applied to SS316L.

Therefore, two identical near-infrared cameras equipped with two different monochromatic interference filters are used. The same scene is accessed through an optical component responsible for splitting the beam into two paths with the same transmission rate. Thus, two images of the same scene are captured at exactly same time but in two distinct wavelengths. The synchronization of data acquisition is ensured by a common trigger to the cameras. Thus, the image sequence captured by the sensors is treated. A couple of images captured at the same time are superimposed. This geometrical manipulation is accessed by a dedicated open-source code library (OpenCV). Next, the temperature of each pixel is calculated following Equation (1) (more details of the assumptions were addressed by Monier et al. [10]).

$$T = \frac{hc}{k_b} \frac{(\lambda_1 - \lambda_2)}{\lambda_1 \lambda_2} \frac{1}{\ln\left(k_{\lambda_1\lambda_2} \frac{Ng_{\lambda_1}}{Ng_{\lambda_2}} \frac{{\lambda_1}^5}{{\lambda_2}^5}\right)} \quad (1)$$

where h is the Planck's constant, c is the light celerity, k_b is the Boltzmann constant, λ_1 and λ_2 are the wavelengths, $Ng_{\lambda 1}$ and $Ng_{\lambda 2}$ are the gray level at respective wavelengths, and $K_{\lambda 1 \lambda 2}$ is the sensitivity coefficient.

2.2. Thermal Measurement Device

Figure 1a shows a schematic of internal component details employed in the thermal measurement equipment conceptualization. A commercial C-Mount cube beamsplitter (reflection/transmission ratio 50/50) equipped with two bandpass filters was used. The project also considered the design to keep the NIR sensors as close as possible to the surface of the beamsplitter's cage, avoiding enlarging the optical path. An external box was designed and manufactured. The two USB connections of the sensors and a single trigger connector are placed on the top side of the device's box. A real picture of the assembled equipment is shown in Figure 1b. The main contribution of this development consists of the miniaturization capability due to the choice of the components, especially the sensors and the beamsplitter. The beam is split into two paths disposed 90° to each other. It allows, beyond facilitating the allocation of sensors, that the thermal images can be generated in a full sensor's resolution (in the current case, 2592 × 1944 pixels). It is worth highlighting its compactivity, assuming the final dimensions of 120 × 57 × 55 mm^3 including the objective lens. The originality of the developed equipment consists both of its small size (allowing the TCP to be embedded) and the low-cost aspect compared to commercial TCP equipment.

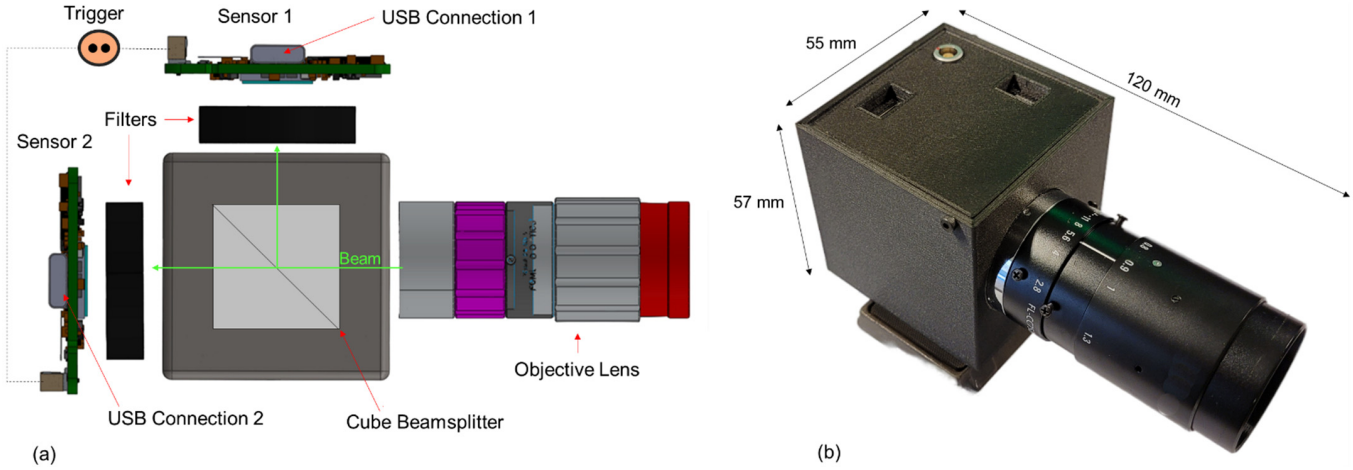

Figure 1. Developed device: (**a**) cage internal components detail under the upper view; (**b**) external view.

2.3. Choice of the Filters and Calibration Procedure

As mentioned in the previous Section 2.1, the right selection for the couple of filters is fundamental. Hence, the upcoming spectrum of the region that would be thermally measured was accessed by using an Ocean Optics HR2000 + CG spectrometer (Orlando, FL, USA). Figure 2 illustrates the results obtained during the welding from the NIR wavelength 600 nm to 1000 nm. Thus, it is important to select some regions where the irradiance is lower, in order to suppress the plasma radiation. It is also relevant to mention that the wavelength range between the couple of filters should not be so distant that it would lead to an enlargement of mean gray level differences, and not so close that it would increase the measurement uncertainties [10]. Considering these statements and the commercially available filters, the ones of 890 nm and 990 nm were chosen. The bandwidth of the filters is 10.0 nm.

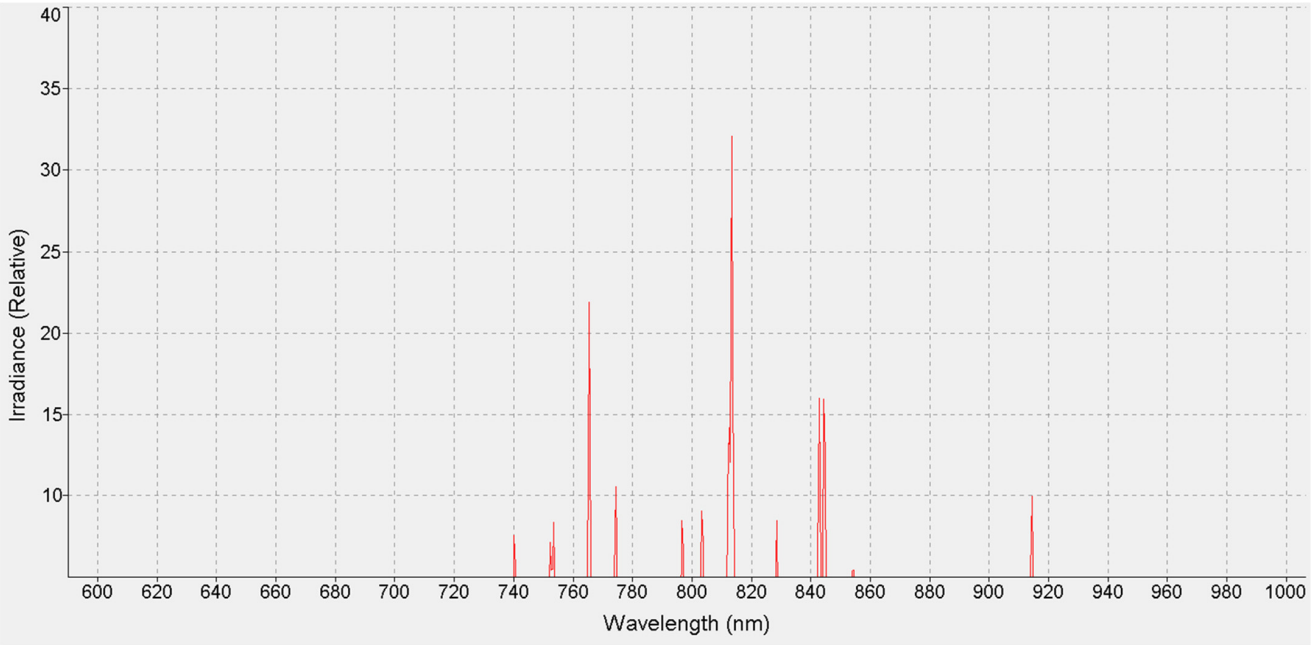

Figure 2. The welding region spectrum obtained for stainless steel 316L, and welding current at 140 A. The curve was plotted by SpectraSuite® version 2.0.

Wójcik et al. [21] highlighted the necessity of being guided by the basic principles of reducing the uncertainty of temperature measurement by thermographic technology in the high-temperature range. Among others, one fundamental is the ability to measure

the true temperature and estimate the effective emissivity. Nevertheless, still according to the authors, thermal radiation of metals is generated by photons resulting from quantum processes in a thin surface layer of about 4 nm thick. Therefore, when the metal is heated to high temperatures, its surface roughness degree, its oxidation by atmospheric oxygen, the presence of impurities, etc., can lead to a substantial change in spectral dependence of the thermal radiation coefficient in comparison with the tabular values given in reference books. Knowing these challenges, one method widely used by many authors [5,20–22] is to source a filament of tungsten whose thermophysical and radiative properties are well known, simplifying the calculation of its true temperature, and thus the effective emissivity. Furthermore, Monier et al. [10] conducted several experiments using pure materials and demonstrated the feasibility of the calibration transposition from the tungsten lamp to liquid metals. Thus, the tungsten filament of an Osram E27 WI 17/G 16A 9V lamp (OSRAM GmbH, München, Germany) was used in this work and can provide a maximum temperature of 2856 K (as the purpose is to measure the temperature of liquids, it is a reasonable approach instead of a blackbody source).

The schematic in Figure 3 illustrates an overview of the calibration procedure. It uses a DC power supply that permits the current selection (current is settled and fixed). Thus, the current is varied within a range that the correspondent temperature will cover the necessary temperature of the application (in this current work, from 1673 K (which corresponds to 316L stainless steel liquidus temperature) to 2856 K (the maximum temperature provided by the lamp)). As the current and voltage outputs are monitored, and the tungsten thermophysical and radiative properties are well known, it is possible to calculate the filament's temperature correlating to its electrical resistance. Therefore, the monochromatic radiances ($L_{\lambda 1}$ and $L_{\lambda 2}$) are calculated at the wavelengths 890 nm and 990 nm, as we know the tungsten filament emissivity at a given temperature. Thus, as the gray level (Ng) is directly related to the photon energy received by the sensor, its relation with the monochromatic radiances can be written by Equation (2). As the exposure time is equally settled for the two sensors, the relation in Equation (3) can be established. Thus, the sensitivity coefficient ($K_{\lambda 1 \lambda 2}$) is found and used in the thermal field computation for the acquired frames. The obtained calibration curve is displayed in Figure 4. The sensitive coefficient must be settled according to the exposure time. As the exposure time of 2 ms was used for the experiments, a $K_{\lambda 1 \lambda 2}$ of 0.328 was fixed. For more information about the procedure, uncertainties, and errors, see [10].

$$Ng_{\lambda} = L_{\lambda} t_{exp} S_{\lambda} \tag{2}$$

where t_{exp} is the exposure time and S_{λ} the sensor sensitivity at wavelength λ.

$$\frac{L_{\lambda 1}}{L_{\lambda 2}} = \frac{Ng_{\lambda 1}}{Ng_{\lambda 2}} \frac{S_{\lambda 1}}{S_{\lambda 2}} = \frac{Ng_{\lambda 1}}{Ng_{\lambda 2}} K_{\lambda 1 \lambda 2} \tag{3}$$

2.4. Experimental Procedure

A schematic drawing of the experimental setup as well as its real picture are presented in Figure 5. A power supply Sincosald TIG AC/DC 400 (Sincosald, Agrate Brianza, Italy) was employed over the current constant mode equipped with a water-cooled torch. The bead-on-plate weldings were carried out on 316L stainless steel plates of 150 × 70 × 3 mm^3. An AWS ER316LSi wire (1.2 mm diameter) was used as low-carbon-grade austenitic stainless steel feedstock. A 2.4 mm diameter tungsten electrode with 2% lanthanum and 30° of grinding angle was used. The electrode–plate working distance was settled to 3 mm. A gas lens ceramic nozzle with an internal diameter of 9.5 mm was employed using pure argon grade 4.5 (99.995% % purity) as shielding gas at 8 L/min. The arc was initiated by lift-arc; the displacement system starts moving 1 s after the arc ignition. The voltage and current signals were acquired using Labjack T7 data acquisition device (LabJack Corporation, Lakewood, CO, USA) at 5000 Hz. A secondary Allied Visio Mako camera positioned at the side of the torch was used to capture images of the wire feeding.

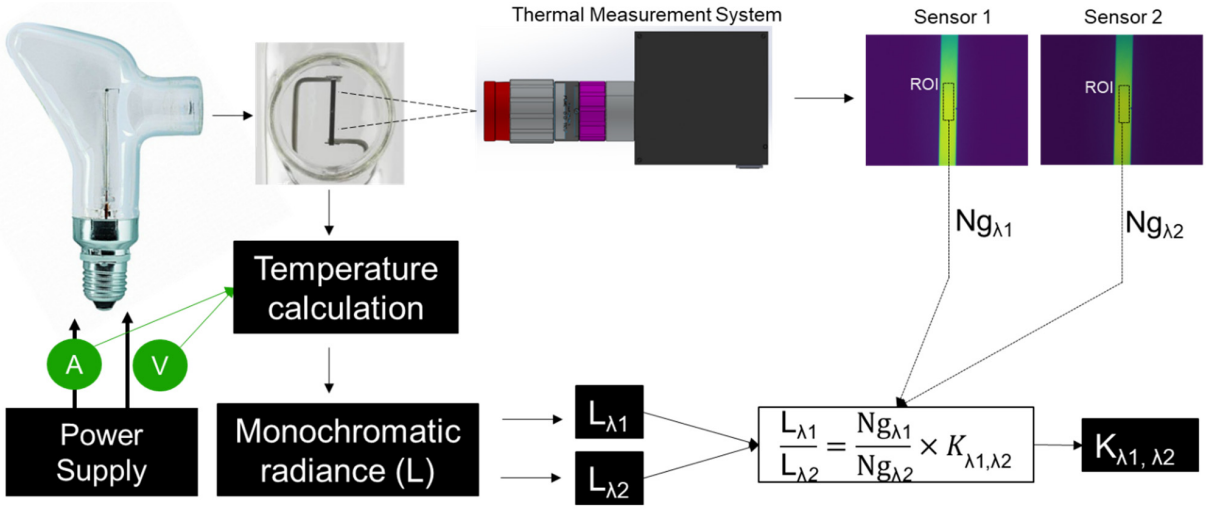

Figure 3. Schematic of the calibration procedure employed to find the sensitivity coefficient for a selected iris diaphragm and couple of filters.

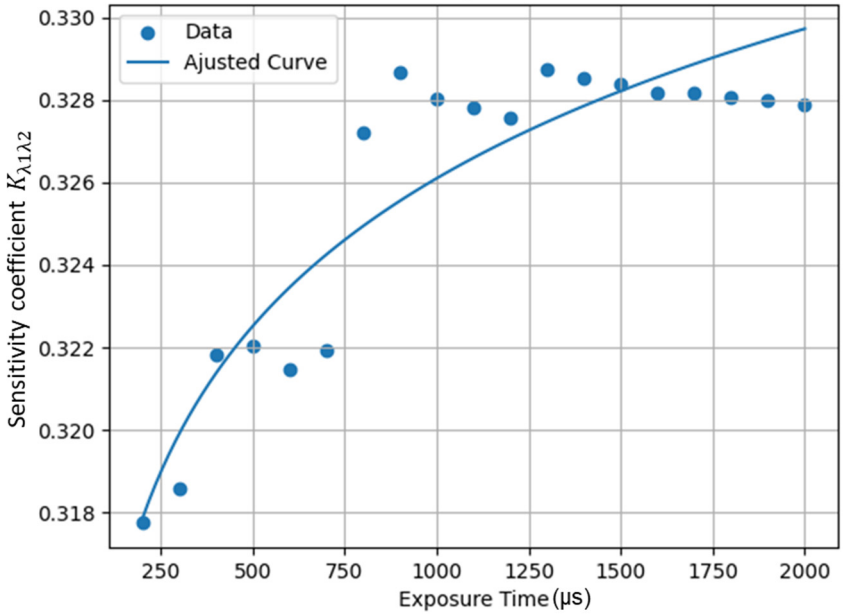

Figure 4. Sensitivity coefficient obtained at a settled exposure time using a 5.8 iris diaphragm and a couple of filters 890/990 nm.

The experiments shown in Table 1 were executed to evaluate the feasibility of using the proposed strategy to monitor the temperature of the rear of the weld pool. In the first parameter condition chosen for Experiment 1, the wire feed was not used (autogenous welding). In this case, a stable weld pool would be expected, simplifying a first assessment of the measuring technique. In Experiment 2, the wire feed was introduced. The first specific aim was to study the influence of the arc and the electrode brightness on the weld pool temperature measurement. For this purpose, the maximum sensor framerate of 80 fps was settled (considering the minimum necessary resolution to cover the weld pool). The idea was to potentialize the visualization of the weld pool's thermal changes when the arc has stopped and the brightness has reduced due to the electrode cooling. Then, a second specific aim was to verify how the metallic transfer type can affect the temperature measurement. It would be expected that an intermittent metallic transfer could provide more perturbation to the weld pool, and thus affect the reflection within it, challenging the thermal measurement. In experiments 3 and 4, the parameters were settled to achieve

bridge and intermittent metallic transfer, respectively. To verify the statement concerning the metallic transfer, a second camera was used and positioned at the side of the torch, making possible the visualization of the wire–weld pool interaction. The geometrical features of the weld beads from experiments 3 and 4 were accessed and correlated to the thermal measurements. Two transversal sections of each weld bead were obtained for the macrograph assessment. The penetration, the width, and the melded zone were measured by using ImageJ® software. As can be seen in Figure 6, a centre line that corresponds to the electrode centre was traced, and the geometrical measurements were performed for each side denominated regions 1 and 2.

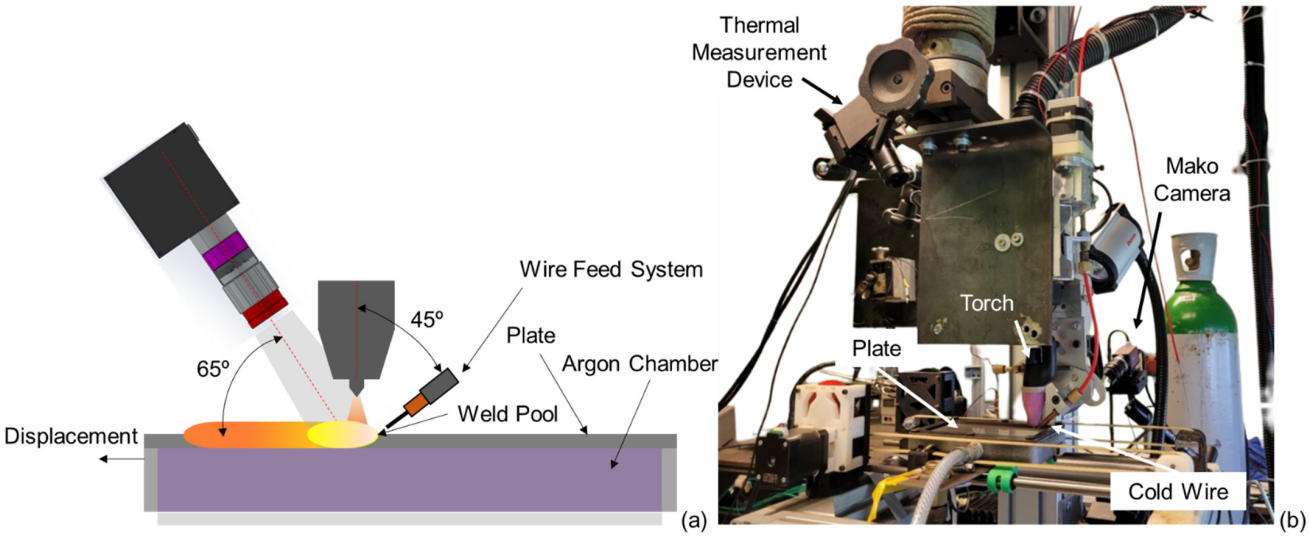

Figure 5. (**a**) Schematic positioning, and (**b**) workbench setup for the experiments.

Table 1. Experimental matrix and its settled and monitored parameters. Travel Speed = 2.9 mm/s (for all experiments); wire feeding angle in relation to the plate surface = 40°.

Experiment Label	Settled Current (A)	Wire Feed Speed (m/min)	Monitored Voltage (V)	Monitored Current (A)	Frame Rate (fps)
1	110	-	8.0 ± 0.1	108.1 ± 0.8	66
2	150	1.5	8.5 ± 0.2	146.6 ± 1	80
3	145	1.5	8.8 ± 0.1	141.1 ± 0.8	66
4	170	1.5	10.1 ± 0.3	167 ± 0.8	66

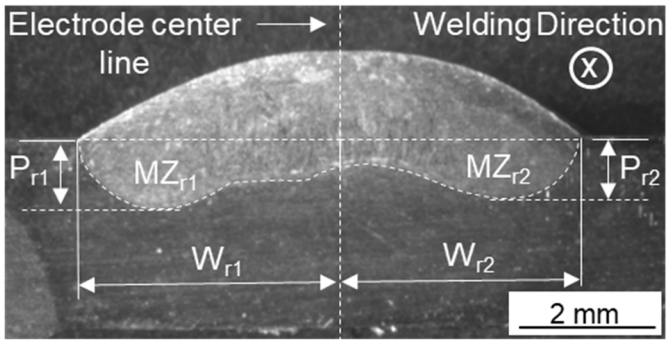

Figure 6. Geometrical features measured for the transversal sections extracted from the weld beads where two regions were divided by the electrode centre line. P = maximum penetration; MZ = melted zone area; W = maximum width; r1 corresponds to region 1, and r2 corresponds to region 2 (the cross-section corresponds to Experiment 4).

2.5. Optical Settings and Temperature Measurement Strategy

Concerning the optical parameters, the 1200 × 1200 pixels resolution was used for the experiments, except in Experiment 2 (due to the increase of FPS, a resolution of 600 × 396 was selected). The exposure time of 2 ms was settled. The system was equipped with an objective of 75 mm focal length and F2.8–32 iris range. The iris diaphragm of 5.6 was kept for all experiments. The thermal system was fixed 0.30 m away from the region of measurement (weld pool). It is worth highlighting the importance of finding the right selection of exposure time and iris opening to work with, especially in the case of this current work. As the equipment was placed with an angle different from 90°, a reasonable field depth is necessary to maintain focus for the entire visible weld pool area (see Figure 7). However, if high values for the iris diaphragm are used, it leads to an increase in the exposure time in order to let enough light go through the sensor to make the acquisition of satisfactory images possible. Two losses can be delineated due to an increase in exposure time. It will reduce the framerate limit, remembering that the video output framerate determines how much time there is available per output frame (a long exposure demands more time), and secondly, it can make moving objects too blurry for the image that is the sensor records light over an extended period in which multiple positions of the object can be detected. Thus, selecting the optical parameters is not trivial. They will also depend on the filters that are being used, as well as the welding parameters. For this work, several experiments were made previously to find them.

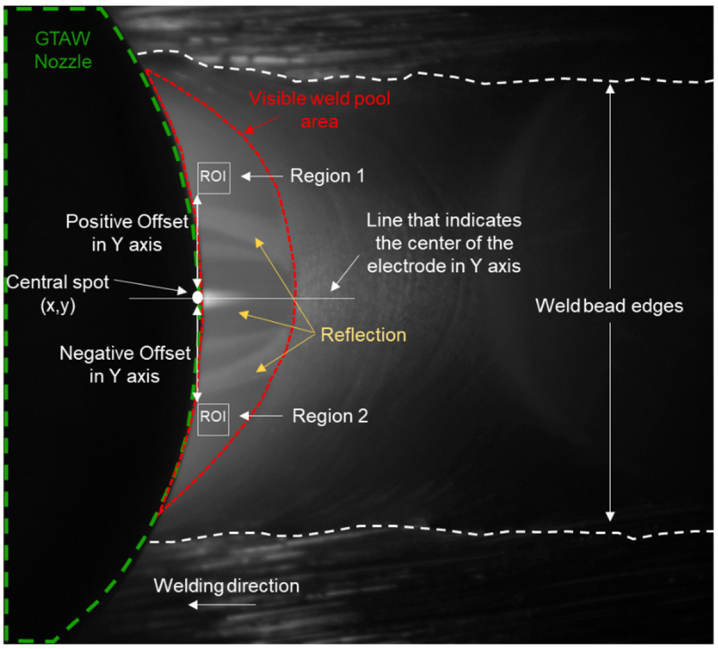

Figure 7. Example of ROIs placement details on a raw image extracted from Experiment 3 using the camera positioning shown in Figure 5.

Regarding the mean temperature analyses, a procedure was followed to select the region of interest (ROI) within the weld pool. It is important to state that all raw images respective to the frames that will be shown in this current work are the ones captured at 890 nm. Figure 7 exemplifies one raw image. As can be seen, dashed lines were traced to make the identification of the elements in the image easy. Among them, the visible weld pool area is of interest for this current study. Within it, it is possible to realize the presence of the reflection coming from the electrode/nozzle. However, for the temperature measurement, these regions should be avoided. Thus, the strategy to position the ROIs consists of delimitating two square ROIs of the same size and placing them within the weld pool. The first step is to define the coordinates of the central spot. This procedure was conducted manually for each experiment considering the weld pool features obtained.

To reach a fair comparison, two ROIs were placed at the same Y coordinate offset from the line that crosses the centre of the electrode. Moreover, the offset was chosen for positioning ROI within the weld pool where there is no presence of reflection coming from the electrode/nozzle. The ROI dimension was also established depending on the weld pool size of each experiment, varying from 44 × 44 to 54 × 54 pixels.

3. Results and Discussion

Figure 8 shows a raw frame of Experiment 1 and its corresponding computed thermal field. At first glance, it may not be immediately clear where the boundaries of the weld pool are in the thermal image. Some regions outside the weld pool appear to have higher temperatures. However, upon examining the raw image, it becomes apparent that these regions correspond to the ones that have higher brightness. Additionally, the weld pool boundaries are clearly visible in the raw image. It can be said that the increase in brightness is due to the light coming from the arc and the electrode. It is important to state that the method used to compute temperatures relies on the gray level of each pixel. Thus, incorrect temperature readings may result from increased gray levels caused by the light of the arc/electrode.

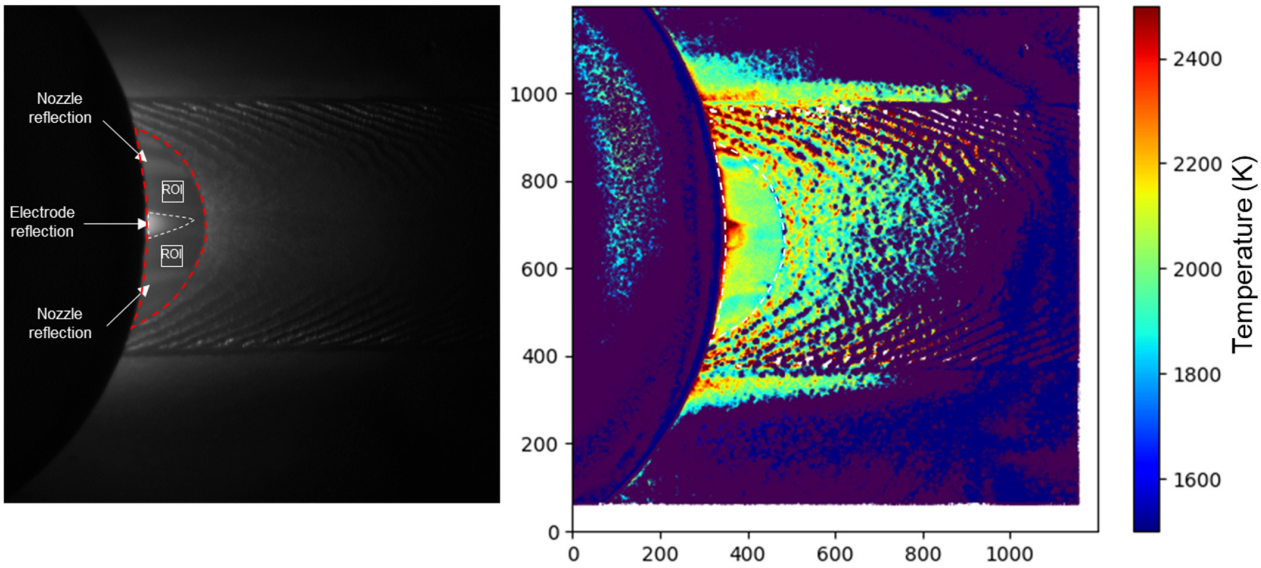

Figure 8. Single raw frame highlighting the reflection within the weld pool and the positioning of the ROIs for Experiment 1 (**left**); thermal field generated from this frame (**right**).

Still considering the raw image in Figure 8, and now focusing only on the area corresponding to the weld pool, the existence of electrode and nozzle reflection can be noted. These reflections are indicated to have higher temperatures in the thermal field and may not reflect the actual temperature of the weld pool. However, there are regions with no reflection incidence where the thermal field could represent the real temperature of the weld pool. Within them, regions of interest (ROIs) were positioned and the mean temperature was calculated by the contribution of each frame. The results are plotted in Figure 9. It can be observed that the mean temperature evolution of both regions is similar, despite having some peaks that will be discussed. However, the usage of some filters on the temperature curve would be possible, improving its visualization, despite the author's preference being to show the raw data separate from the temperature measurement. Even with these peaks, the raw temperature curves of the ROIs are practically superimposed. Particularly in this experiment, large mean temperature variations comparing the ROIs would be expected, as they were positioned symmetrically from the electrode centre line, and a stable welding condition was reached. This is supported by data extracted from various sources, including raw images, voltage/current signals, and the weld bead appearance. Nevertheless, it could still be questioned whether the luminosity of the arc and electrode would affect the actual

temperature value within the ROIs. Furthermore, the effect of the absorption could also lead to the misreading of the temperature.

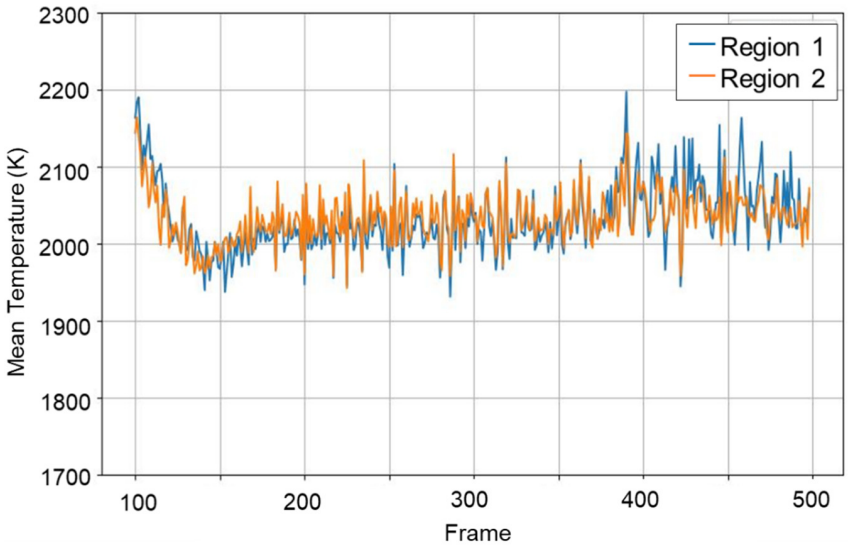

Figure 9. Mean temperature of ROIs 1 and 2 calculated for each frame of Experiment 1.

To evaluate the influence of the arc and the electrode brightness on the weld pool temperature measurement (first specific objective), four frames extracted from Experiment 2 are displayed in Figure 10. The top frames are raw images, while the bottom ones are their respective thermal field. This sequence represents moments before and after the arc has been interrupted. The interruption occurred between frames 506 and 508, and the time between two consecutive frames is about 12.5 ms. Looking at frames 511 and 514, it is possible to see the electrode cooling by the reduction of its reflected light at the weld pool. As previously stated in Experiment 1, there is also reflection incidence in Experiment 2, as seen in Figure 11. However, it takes up a different location and configuration. In Experiment 2, the wire feed was added and thus the weld pool assumed a different shape. Therefore, two ROIs were positioned at a higher Y offset value compared to Experiment 1. Figure 12a shows the mean temperature evolution of the ROIs during the opening arc time until a few milliseconds after the arc's shutdown.

Likewise, Figure 12b displays in detail the mean temperature of frames 506 to 514. It is possible to note a slight temperature decrease when the arc has ceased between frames 506 and 508. There are two possible explanations for this observation. Firstly, the light from the arc could have reduced over the weld pool, making the region of interest (ROI) appear less bright, leading to an error in temperature computation. Secondly, the temperature might have actually dropped because the arc has shut down. In other words, the heat source's interruption leads to a decrease in the weld pool's temperature surface within a short period. If the light from the arc and the electrode could affect the temperature measurement of the weld pool within the ROIs, then we would expect to see a decrease in temperature from frame 511 to 514 as the light from the electrode reduces. However, the temperature increased even though the light from the electrode had reduced. It is crucial to state that even after the arc's shutdown, convection and heating mass transfer still occur within the weld pool. This observation implies that the hypothesis that the arc light could lead to misreading of the temperature loses weight.

To evaluate the impact of the metallic transfer on the temperature measurement following the proposed strategy, the results from Experiment 3 (bridge metallic transfer) and 4 (intermittent metallic transfer) will be discussed. Figure 13 illustrates a sequence of frames captured by a camera positioned sideward from the nozzle. In addition, the voltage signal is displayed in Figure 14. As the trigger signal that was sent to the sensor was recorded by the acquisition system, it was possible to synchronize and thus find the exact time of

each captured frame of both cameras (400 representative frames were captured in each experiment for the analyses). The voltage signal shows the presence of ripples when the metallic transfer assumes an intermittent condition. It can be explained by the instantaneous change in weld pool volume that leads to variations in the arc length. In addition, the arc can deflect cyclically and part of it moves from the cold-wire extreme/pool surface to the cold-wire surface. This behaviour concerning metallic transfer is also discussed by other authors [23,24]. Regarding the thermal system, a sequence of raw frames from Experiment 3 and 4 are displayed in Figure 15 which corresponds to the same instants as those shown in Figure 13. Both experiments exhibit the presence of reflection within the weld pool. However, in Experiment 4, due to the fluctuating shape and volume of the weld pool caused by the wire feed interruption, the size of the reflection varies significantly. For instance, comparing the frames 165 and 166 of Experiment 4 in Figure 15, there is an observable increase/decrease in the reflection's size. Nevertheless, there are still areas without reflection where the ROIs (regions of interest) could be positioned.

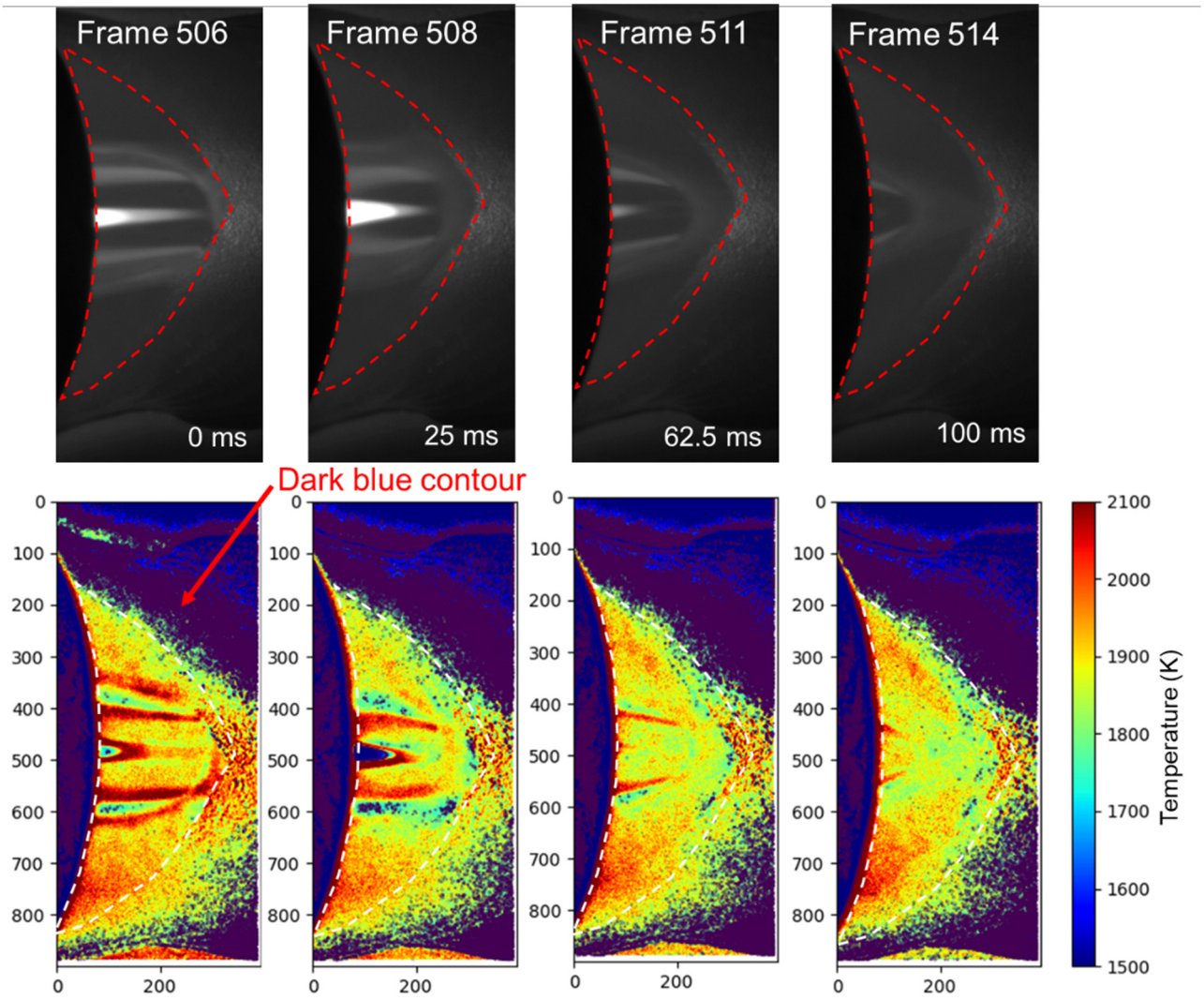

Figure 10. Sequence of frames that represents moments before and after the arc has been interrupted (the interruption occurred between frames 506 and 508). At the (**top**) are raw images, while at the (**bottom**) are their respective thermal fields. The dark blue contour was imposed by the software and corresponds to 316L stainless steel liquidus temperature. The time was imposed in the frames using the frame 506 as the starting reference.

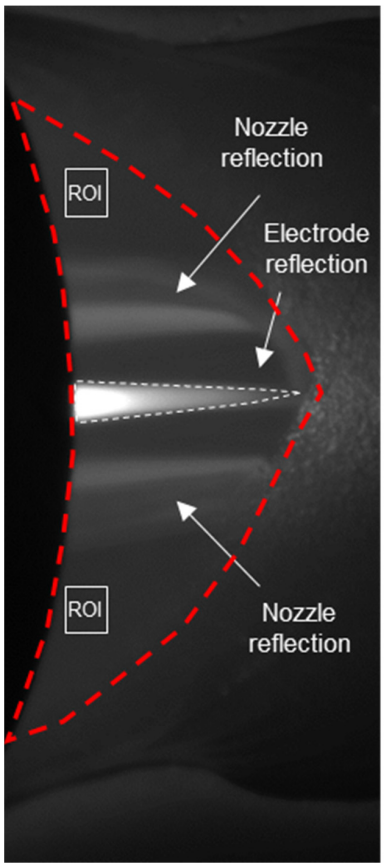

Figure 11. Raw frame extracted from Experiment 2 showing the position of the reflection and the positioning of the ROIs within the weld pool.

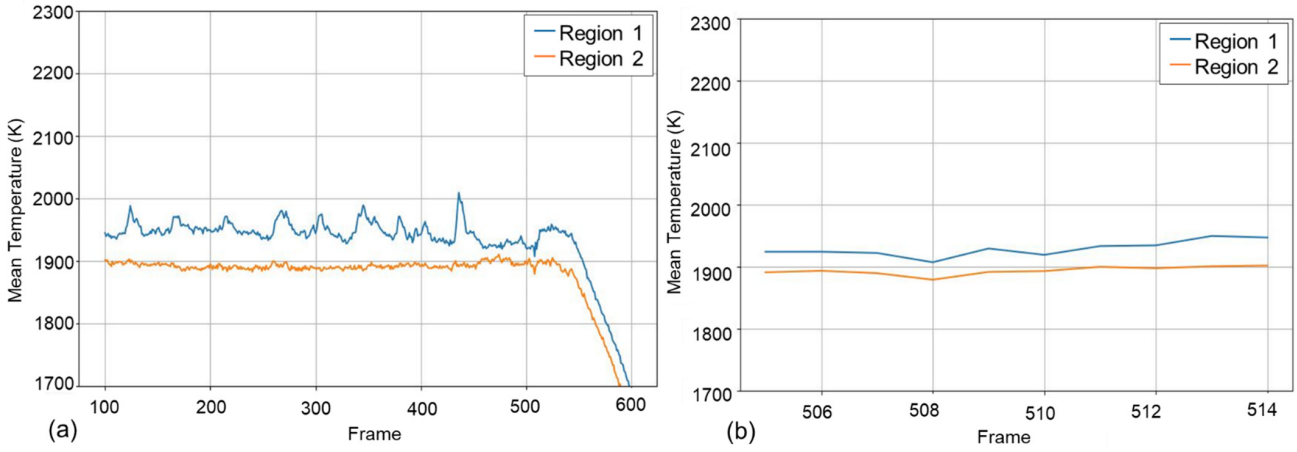

Figure 12. Mean temperature of ROIs 1 and 2 in Figure 11 calculated for each frame of Experiment 2. (**a**) from the instant that the welding assumed a regime condition to a few milliseconds after the arc's shutdown; (**b**) moments before and after the arc has been interrupted.

To facilitate the correlation between the thermal measurement and the geometrical features, Figures 15 and 16 combine the surface aspect of the weld bead, the corresponding two cross-section macrographs, and also the evolution of the mean temperature along the welding for the respective ROIs of Figure 15. A white dashed line corresponding to the electrode centre was drawn and regions 1 and 2 were indicated. At first glance looking at Figure 16, it is possible to perceive a good appearance of the weld bead, although followed by small fluctuations along its borders (seeming minor ripples) for Experiment 3. However, a slight difference in the weld bead penetration profiles can be observed comparing regions

1 and 2 at the cross-sections. The penetration, width, and melted zone results are quantified in Table 2. As the penetration profiles were very similar in both sections, the features were measured only for Section 1. There is an increase in the penetration and the melted zone for region 1 compared to region 2, while the width remains very close. Some hypotheses can be pointed out to justify this difference, such as a misalignment between the entrance of wire into the weld pool and the electrode centre. It could have caused an arc deviation and thus heating differences provided to regions 1 and 2. Therefore, independent of the causes that may have affected the heating distribution within the weld pool, it is possible to visualize a higher mean temperature for the ROI positioned in region 1 compared to region 2 during the welding time, registered by the thermal system (both from the Figure 15 and Table 2). From the thermal point of view, higher heating leads to melt power growth and can justify higher values of melted zone and penetration in region 1.

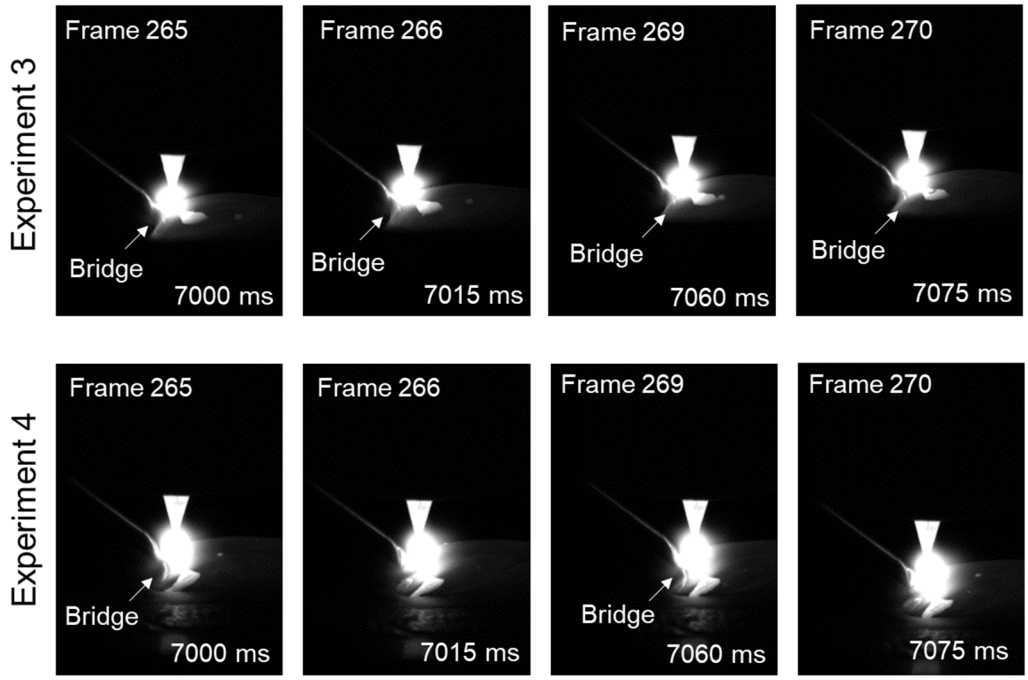

Figure 13. Details of the metallic transfer showing the bridge transfer in Experiment 3 and the intermittent transfer in Experiment 4.

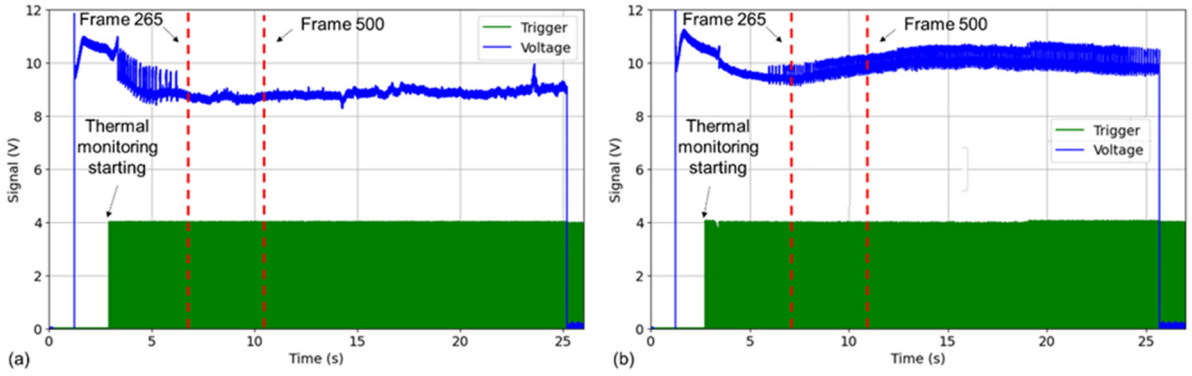

Figure 14. Voltage and trigger signals acquired for Experiment 3 (**a**) and 4 (**b**), as well as the positioning of captured frames.

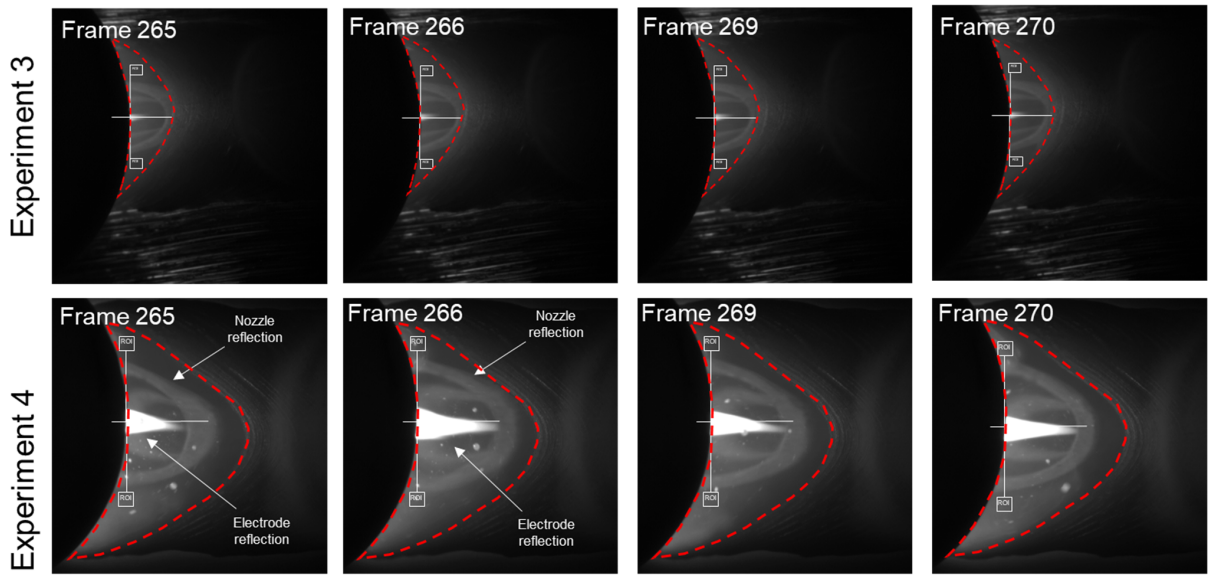

Figure 15. Sequence of raw frames extracted from Experiment 3 and 4 showing the position of ROIs and highlighting the variation of reflection's size at frames 265 and 266 in Experiment 4.

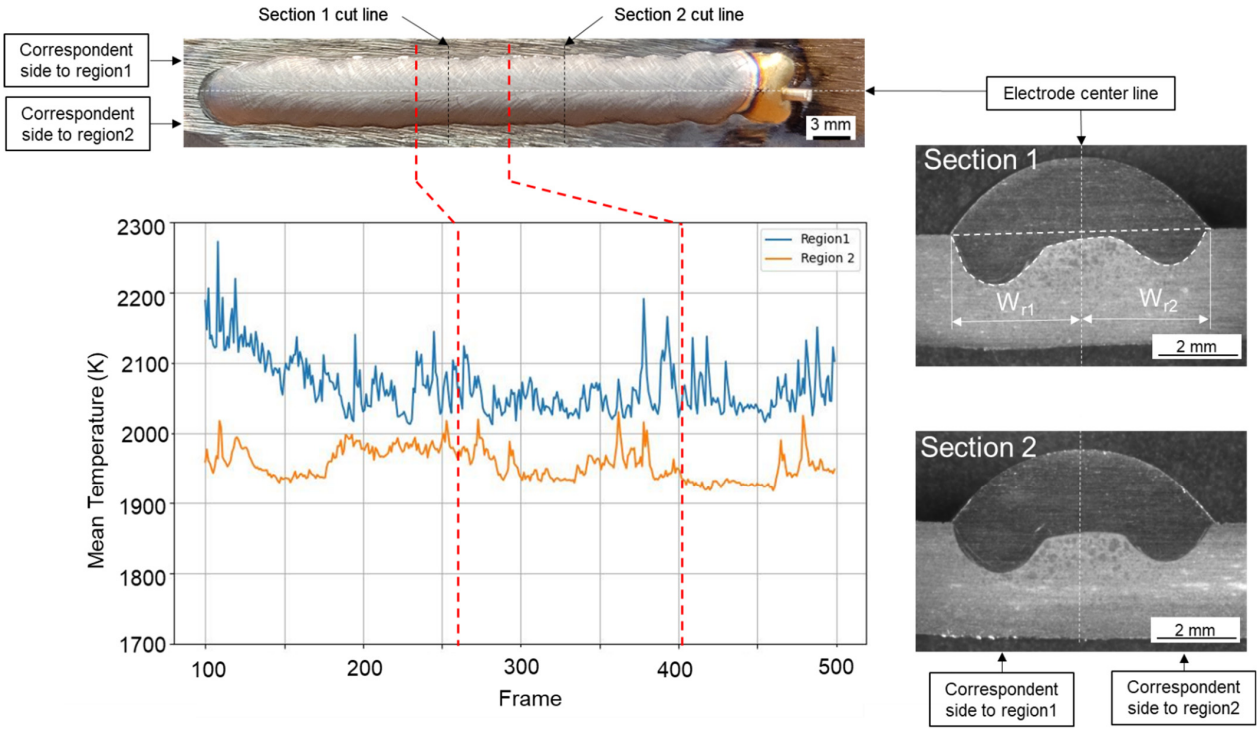

Figure 16. Schematic that presents the combined aspects of the surface appearance of the weld bead, its correspondent two cross-section macrographs, and also the evolution of the mean temperature along the welding for the respective ROIs of Figure 15 for Experiment 3.

Still looking at the mean temperature curves in Figure 16, the appearance of fluctuations in the mean temperature and some moments when these fluctuations increase/decrease abruptly can also be noted. It is important to mention that the presence of oxides supernatant in the weld pool can punctually affect the measurement leading to some peak or downfall in the temperature. In addition, the coupling of the arc and weld pool surface depends on how the weld pool experiences motion, as well as by the presence of oxides. Thus, quick deviations or perturbations of the arc may happen (it is already known the intrinsic sensibility of the GTAW process) that can cause swift changes in the surface's thermal field

and then the heat flux. The thermal field within the weld pool is a complex phenomenon that depends on physical and chemical transformations and heat mass transfer.

Table 2. Quantification of penetration, width, melted zone, and mean temperature (using the interval from frames 260 to 400) for Experiment 3 and 4, according to the sketch of Figure 6.

Feature	Experiment 3		Experiment 4	
	Region 1	Region 2	Region 1	Region 2
Penetration (mm)	1.2	0.9	1.0	0.9
Width (mm)	3.3	3.2	3.9	3.5
Melted Zone (mm^2)	2.4	1.4	2.8	2.2
Mean Temperature (K)	2054	1957	2068	1800

Following the same approach, Figure 17 displays the surface appearance of the weld bead, and its corresponding two cross-section macrographs, and also the evolution of the mean temperature during the welding for Experiment 4. Using the measured features of Table 2, it is possible to indicate the increase mainly for the width and melted zone of region 1 compared to region 2. Obtaining the mean temperature, a significant difference can be stated comparing both regions during all welding time. Succeeding the same thermal affirmation given for Experiment 3, the higher temperature could justify the growth of the melted zone and width in Experiment 4. In addition, what calls for attention is the major fluctuations of the mean temperature in region 1 while it practically assumes a linear trend in region 2 despite some punctual peaks. Additionally, looking now at the weld bead appearance, it can be noted that the borders along the weld bead of region 2 tended to assume features with fewer variations. Blue dashed lines equally spaced from the electrode centre line (white dashed) were charted to facilitate the visualization. On the other hand, more deviations can be realized regarding the weld bead borders in region 2. Furthermore, a slight enlargement of the weld bead around the frame 260 is followed by an increase in the temperature. These insights suggest a correlation between the weld pool temperature and the geometrical features of the resulting weld bead.

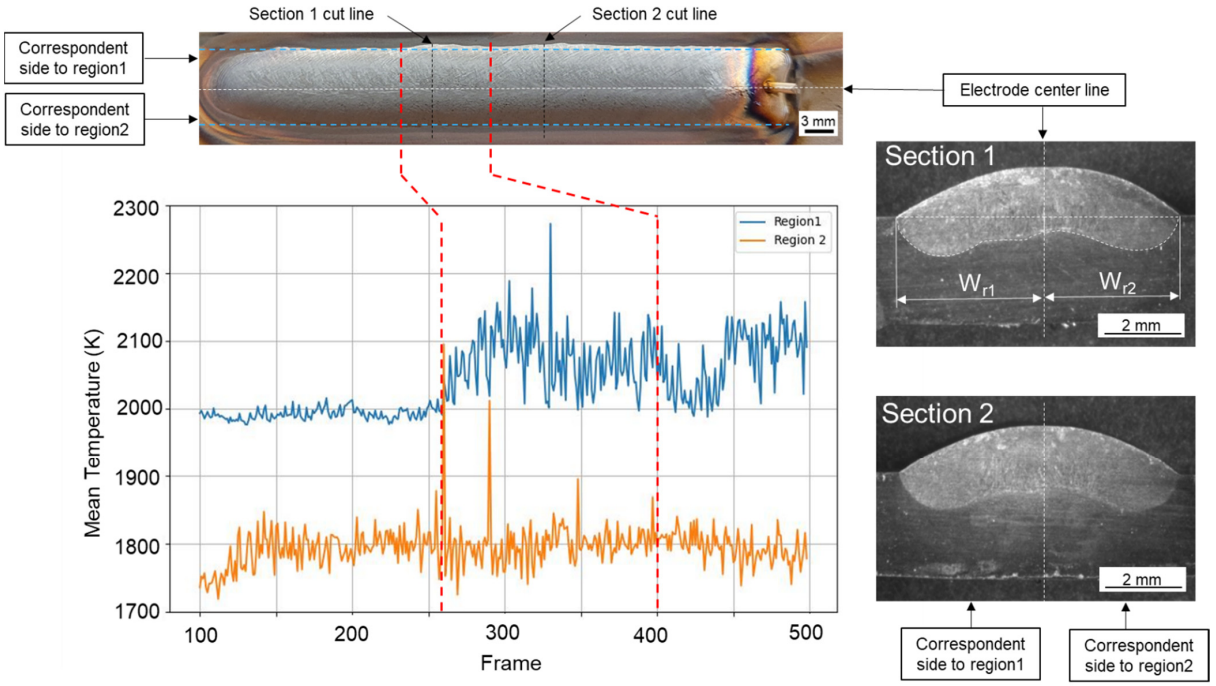

Figure 17. Schematic that presents the combined aspects of the surface appearance of the weld bead, its corresponding two cross-section macrographs, and also the evolution of the mean temperature along the welding for the respective ROIs of Figure 15 for Experiment 4.

4. General Discussion

Overall, the constant search for strategies to ensure the quality of the welded joint in automatic welding processes is unanimous. However, some intrinsic features such as the penetration and volume of molten material take place beneath workpieces and are not readily observable during the manufacturing process, presenting a challenge for in situ non-intrusive monitoring on the surface. The complexity of factors that govern the weld bead formation in welding is remarkable. In summary, Jorge et al. [25] updated a hierarchical representation of the weld bead formation in the GMAW process. In fact, despite such differences and particularities that can lead the GTAW process to have distinct mechanisms, it can be affirmed that the weld bead formation is ruled by thermal and mechanical effects. According to Yu et al. [16], the temperature field reflects the heating and melting and thus provides certain information about the penetration. However, they also mentioned that it is not clear if there is an exact mapping between the temperature field and the penetration.

The findings of this current work firstly demonstrate the feasibility of using the developed system to access the thermal field of the rear weld pool, although the reflection must impose the necessity of a ROI selection within the weld pool. The presence of the reflection is also discussed by other authors [26,27]. What is interesting to mention is that they also used the reflection of the arc/electrode as a source of data for a penetration prediction employing deep learning. In fact, looking at the experiments of this current work, the reflection feature changes depending on the welding parameters were also stated, although it was not the scope to evaluate these changes. Anyway, it is possible to perceive the potentialities given by the advent of AI. In future work, the authors intend to use strategies of deep learning segmentation to select the ROI in order to better take advantage of the thermal field. As can be seen in Figure 18, the regions of interest must not have to assume a square shape. It could be selected by a segmentation AI algorithm, hypothetically illustrated by the black dashed lines. In addition, the temperature distribution inside the ROI could reveal details of movements of liquid patterns, becoming another important source of data. According to Yu et al. [16], using the transfer learning can improve the accuracy through more effectively extracting all possible patterns in the data.

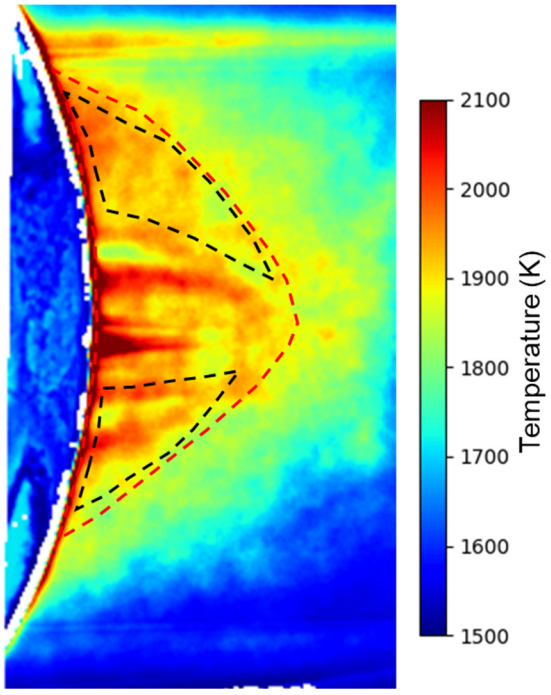

Figure 18. Example of the mean thermal field computed for 400 frames. The dashed red line indicates the weld pool edges and the dashed black line's hypothetical ROIs available for thermal analyses.

Secondly, a correlation between the mean temperature measured by the method proposed in this work and the weld bead features was found. In the last half century, researchers have focused on finding promising real-time observable phenomena and correlating them to weld beads using technics such as instant and/or dynamic weld pool images, acoustic monitoring, and welding electrical signals. In the field of weld pool observation, the findings demonstrate that the mean temperature can be a promising method to indicate geometrical changes in the weld bead. Further experiments will be proposed in the future, especially to verify the current strategy applied to welding joints. For instance, in a groove, it is expected that weld bead defects (such as lack of fusion or geometric deviations) can be predicted by the weld pool temperature during the welding. As verified, a difference in the mean temperature within two regions equally spaced from the electrode centre line can lead to differences in melted zone, width, or penetration.

Last but not least, the application of the proposed approach will depend on the welding condition in which the weld pool features might change depending on the welding parameters, joint type, and material. The large temperature gradients in the molten pool and many driving forces acting simultaneously can lead to surface flow patterns and thus variable temperature fields during the welding in the GTAW process, as stated by Blanc et al. [28]. In such cases, if the current strategy is adopted, a careful framerate selection should be considered, as well as the number of frames to be obtained for the significance of the mean temperature within the ROI. It is also important to mention that in the experiments of this work, the weld pool assumed a stable condition, i.e., no huge geometrical deviations along the welding that could be caused by a change in the current level (pulsed current), transversal oscillation of the torch, or even the usage of dynamic cold wire feed systems. They could increase the weld pool surface perturbations (waves) and might challenge the use of the current strategy due to the difficulty of positioning the ROIs by the presence of reflections and/or high surface curvatures, interfering with the temperature measurement. Still considering the trouble of ROI's positioning, the joint can directly impose an obstacle where the reflection can capture a massive area over the rear of the weld pool, for instance, in narrow gaps. Finally, the rear weld pool monitoring can be extended to other materials, since the emissivity behaviour of the metal liquid is carefully checked allowing for the application of a gray body assumption. However the purity of the material should be considered, that is, the lesser the purity of the material (for example carbon steels), the higher the amount of oxides' supernatant in the weld pool, which can lead to the temperature misreading by the current strategy due to its high emissivity change. The positive highlight is that with the advent of IA, there are already strategies for object detection in images which are seen by authors to overcome the challenges due to oxides. Before extracting the mean temperature of a certain region of interest, the oxide island could be predicted, thus not taking into account its temperature. Hence, a deep evaluation concerning all of these potential limitations is necessary and they will be the object of study in future work.

5. Conclusions

The global objective of this work was to evaluate the feasibility and detect potentialities of accessing the thermal field from the rear weld pool next to the arc radiation in the GTAW process by using in-house developed equipment. In addition, there were two specific goals, which were to study the influence of the arc and the electrode brightness, as well as to verify the effect of the metallic transfer on the weld pool thermal measurement. Given the global and specific objectives, the following conclusions have been drawn:

- A compact thermal imaging equipment was developed based on the two-colour pyrometry principle and its feasibility to access the thermal field from the rear of the weld pool was demonstrated.
- The arc/electrode brightness did not affect the temperature measurement following the proposed strategy.

- The presence of the arc and/or nozzle reflection within the weld pool can assume different formats and sizes depending on the camera positioning and the weld pool's shape. However, there are regions in which the actual weld pool temperature can be accessed.
- The rear weld pool thermal field is an important source of data that can provide hints about the weld bead features. The mean temperature can indicate geometrical changes in the weld bead. Moreover, the technique has the potential to be used for promising real-time process monitoring.

Author Contributions: Conceptualization: V.L.J., I.B., F.S. and C.B.; methodology: V.L.J., F.S. and C.B.; material preparation and data collection: V.L.J.; investigation: V.L.J.; validation: V.L.J., I.B., F.S. and C.B.; data curation: V.L.J.; writing—original draft preparation: V.L.J.; writing—review and editing: V.L.J., I.B., F.S. and C.B.; supervision: F.S. and C.B., project administration: C.B. All authors have read and agreed to the published version of the manuscript.

Funding: This work was supported by Électricité de France—EDF (Grant No. DOS177126—Bpi project Weldia).

Data Availability Statement: The datasets generated during and/or analyzed during the current study are available from the corresponding author on reasonable request.

Acknowledgments: The authors would like to thank the University of Montpellier, France, for their generous support in providing laboratory infrastructure and essential materials, which significantly contributed to the success of this research.

Conflicts of Interest: The authors, from educational and research state institutions, declare that the research was conducted in the absence of any commercial or financial relationships that could be construed as a potential conflict of interest.

References

1. David, S.A.; Babu, S.S.; Vitek, J.M. Welding: Solidification and microstructure. *JOM* **2003**, *55*, 14–20. [CrossRef]
2. Yu, R.; Huang, Y.; Peng, Y.; Wang, K. Monitoring of butt weld penetration based on infrared sensing and improved histograms of oriented gradients. *J. Mater. Res. Technol.* **2023**, *22*, 3280e93. [CrossRef]
3. Yu, R.; Huang, Y.; Qiu, S.; Peng, Y.; Wang, K. Welding Quality Detection for Variable Groove Weldments Based on Infrared Sensor and Artificial Neural Network. *Metals* **2022**, *12*, 2124. [CrossRef]
4. Yu, R.; Han, J.; Bai, L.; Zhao, Z. Identification of butt welded joint penetration based on infrared thermal imaging. *J. Mater. Res. Technol.* **2021**, *12*, 1486–1495. [CrossRef]
5. Schöpp, H.; Sperl, A.; Kozakov, R.; Gött, G.; Uhrlandt, D.; Wilhelm, G. Temperature and emissivity determination of liquid steel S235. *J. Phys. D Appl. Phys.* **2012**, *45*, 235203. [CrossRef]
6. Coniglio, N.; Mathieu, A.; Aubreton, O.; Stolz, C. Weld pool surface temperature measurement from polarization state of thermal emission. *Quant. InfraRed Thermogr. J.* **2016**, *11*, 83–93. [CrossRef]
7. Muller, M.; Fabbro, R.; El-Rabii, H.; Hirano, K. Temperature measurement of laser-heated metals in highly oxidizing environment using 2D single-band and spectral pyrometry. *J. Laser Appl.* **2012**, *24*, 022006. [CrossRef]
8. Yu, R.; Guo, S.; Huang, Y.; Wang, L.; Peng, Y.; Wang, K. Measurement of weld penetration for variable-groove weldment using dual-band imaging and neural network. *J. Mater. Res. Technol.* **2023**, *24*, 2640–2652. [CrossRef]
9. Myers, A.J.; Quirarte, G.; Ogoke, F.; Lane, B.M.; Uddin, S.Z.; Farimani, A.B.; Beuth, J.L.; Malen, J.A. High-resolution melt pool thermal imaging for metals additive manufacturing using the two-color method with a color camera. *Addit. Manuf.* **2023**, *73*, 103663. [CrossRef]
10. Monier, R.; Thumerel, F.; Chapuis, J.; Soulié, F.; Bordreuil, C. Liquid metals surface temperature fields measurements with a two-colour pyrometer. *Measurement* **2017**, *101*, 0263–2241. [CrossRef]
11. Richter, A.; Gehling, T.; Treutler, K.; Wesling, V.; Rembe, C. Real-time measurement of temperature and volume of the weld pool in wire-arc additive manufacturing. *Meas. Sens.* **2021**, *17*, 100060. [CrossRef]
12. Schwarzkopf, K.; Rothfelder, R.; Rasch, M.; Schmidt, M. Two-Color-Thermography for Temperature Determination in Laser Beam Welding of Low-Melting Materials. *Sensors* **2023**, *23*, 4908. [CrossRef]
13. Ngo Huu, M.; Nguyen Van, A.; Nguyen Van, T.; Tran Hai, D.; Nguyen Van, T.; Nguyen Tien, D.; Nguyen, T.-H. Material Flow Behavior on Weld Pool Surface in Plasma Arc Welding Process Considering Dominant Driving Forces. *Appl. Sci.* **2020**, *10*, 3569. [CrossRef]
14. Monier, R.; Thumerel, F.; Chapuis, J.; Gilles, P.; Soulié, F.; Bordreuil, C. In Situ Experimental Measurement of Temperature Field and Surface Tension during Pulsed GMAW. *Weld. World* **2016**, *60*, 1021–1028. [CrossRef]

15. Myers, A.J.; Quirarte, G.; Beuth, J.L.; Malen, J.A. Two-color thermal imaging of the melt pool in powder-blown laser-directed energy deposition. *Addit. Manuf.* **2023**, *78*, 103855. [CrossRef]
16. Yu, R.; Cao, Y.; Chen, H.; Ye, Q.; Zhang, Y. Deep learning based real-time and in-situ monitoring of weld penetration: Where we are and what are needed revolutionary solutions. *J. Manuf. Process.* **2023**, *93*, 15–46. [CrossRef]
17. Yu, R.; He, H.; Han, J.; Bai, L.; Zhao, Z.; Lu, J. Monitoring of back bead penetration based on temperature sensing and deep learning. *Measurement* **2022**, *188*, 110410. [CrossRef]
18. Buongiorno, D.; Prunella, M.; Grossi, S.; Hussain, S.M.; Rennola, A.; Longo, N.; Di Stefano, G.; Bevilacqua, V.; Brunetti, A. Inline Defective Laser Weld Identification by Processing Thermal Image Sequences with Machine and Deep Learning Techniques. *Appl. Sci.* **2022**, *12*, 6455. [CrossRef]
19. Knaak, C.; Von Eßen, J.; Kröger, M.; Schulze, F.; Abels, P.; Gillner, A. A Spatio-Temporal Ensemble Deep Learning Architecture for Real-Time Defect Detection during Laser Welding on Low Power Embedded Computing Boards. *Sensors* **2021**, *21*, 4205. [CrossRef] [PubMed]
20. Devesse, W.; De Baere, D.; Guillaume, P. High Resolution Temperature Measurement of Liquid Stainless Steel Using Hyperspectral Imaging. *Sensors* **2017**, *17*, 91. [CrossRef]
21. Wójcik, W.; Firago, V.; Smolarz, A.; Shedreyeva, I.; Yeraliyeva, B. Multispectral High Temperature Thermography. *Sensors* **2022**, *22*, 742. [CrossRef] [PubMed]
22. Hofmeister, W.; Griffith, M. Solidification in direct metal deposition by LENS processing. *JOM* **2001**, *53*, 30–34. [CrossRef]
23. Silva, G.R.H.; Riffel, K.C.; Okuyama, M.P.; Dalpiaz, G. Effect of dynamic wire in the GTAW process. *J. Mater. Process. Technol.* **2019**, *269*, 91–101. [CrossRef]
24. Jorge, V.L.; Scotti, F.M.; Reis, R.P.; Scotti, A. The effect of pulsed cold-wire feeding on the performance of spray GMAW. *Int. J. Adv. Manuf. Technol.* **2020**, *107*, 3485–3498. [CrossRef]
25. Jorge, V.L.; Scotti, F.M.; Reis, R.P.; Scotti, A. The potential of wire feed pulsation to influence factors that govern weld penetration in GMA welding. *Int. J. Adv. Manuf. Technol.* **2020**, *110*, 2685–2701. [CrossRef]
26. Zhang, Z.; Wen, G.; Chen, S. Weld image deep learning-based on-line defects detection using convolutional neural networks for Al alloy in robotic arc welding. *J. Manuf. Process.* **2019**, *45*, 208–216. [CrossRef]
27. Feng, Y.; Chen, Z.; Wang, D.; Chen, J.; Feng, Z. Deep Welding: A deep learning enhanced approach to GTAW using multisource sensing images. *IEEE Trans. Ind. Inf.* **2019**, *16*, 465–474. [CrossRef]
28. Blanc, N.; Boutin, T.; Bendaoud, I.; Soulié, F.; Bordreuil, C. Proper orthogonal decomposition analysis of variable temperature field during gas tungsten arc welding. *Phys. Fluids* **2021**, *33*, 125123. [CrossRef]